ACSNANO

www.acsnano.org

ARTICLE

Bifunctional Atomically Dispersed Mo–N_2/C Nanosheets Boost Lithium Sulfide Deposition/Decomposition for Stable Lithium–Sulfur Batteries

Feng Ma, Yangyang Wan, Xiaoming Wang, Xinchao Wang, Jiashun Liang, Zhengpei Miao, Tanyuan Wang, Cheng Ma, Gang Lu, Jiantao Han, Yunhui Huang, and Qing Li*

Cite This: *ACS Nano* 2020, 14, 10115–10126

Read Online

ACCESS | Metrics & More | Article Recommendations | Supporting Information

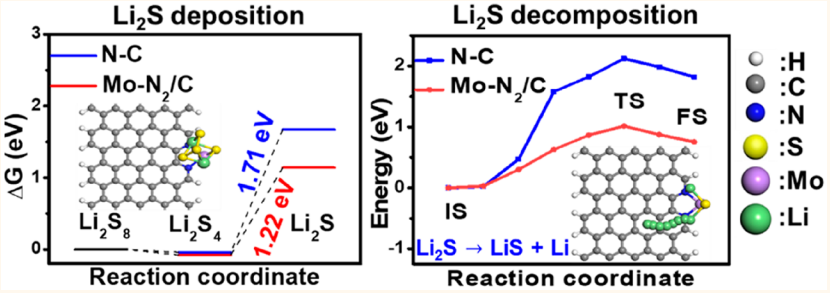

ABSTRACT: **The sluggish kinetics of lithium polysulfides (LiPS) transformation is recognized as the main obstacle against the practical applications of the lithium–sulfur (Li–S) battery. Inspired by molybdoenzymes in biological catalysis with stable Mo–S bonds, porous Mo–N–C nanosheets with atomically dispersed Mo–N_2/C sites are developed as a S cathode to boost the LiPS adsorption and conversion for Li–S batteries. Thanks to its high intrinsic activity and the Mo–N_2/C coordination structure, the rate capability and cycling stability of S/Mo–N–C are greatly improved compared with S/N–C due to the accelerated kinetics and suppressed shuttle effect. The S/Mo–N–C delivers a high reversible capacity of 743.9 mAh g^{-1} at 5 C rate and an extremely low capacity decay rate of 0.018% per cycle after 550 cycles at 2 C rate, outperforming most of the reported cathode materials. Density functional theory calculations suggest that the Mo–N_2/C sites can bifunctionally lower the activation energy for Li_2S_4 to Li_2S conversion and the decomposition barrier of Li_2S, accounting for its inherently high activity toward LiPS transformation.**

KEYWORDS: *Li–S battery, lithium polysulfide conversion, atomically dispersed catalyst, energy storage, electrocatalysis*

The increasing environmental problems and demands for energy consumption call for sustainable energy storage devices with a high energy density and long lifespan. Presently, the commercial lithium-ion batteries (LIBs) cannot satisfy the growing demands for clean energy sources owing to its limited capacity and energy density.[1−4] The lithium–sulfur (Li–S) battery with outstanding theoretical capacity (1675 mAh g^{-1}) and energy density (2600 Whkg^{-1}) has been regarded as a promising candidate for the next-generation energy storage devices beyond LIBs.[5−9] However, several obstacles strictly hinder its practical applications. The sluggish kinetics of Li polysulfide (LiPS) intermediates (Li_2S_x, $2 \le x \le 8$) transformation along with the insulating nature of S and the discharge product Li_2S hinder the efficient electron transportation and damage the successive redox conversion of S_8/Li_2S, leading to a limited capacity, large polarization, and low S utilization.[10−17] Meanwhile, the highly soluble LiPS can diffuse to anode and be chemically reduced from long-chain Li_2S_x ($4 \le x \le 8$) to short-chain ones ($2 \le x < 4$), resulting in a shuttle effect

Received: April 21, 2020
Accepted: July 22, 2020
Published: July 22, 2020

https://dx.doi.org/10.1021/acsnano.0c03325
ACS Nano 2020, 14, 10115–10126

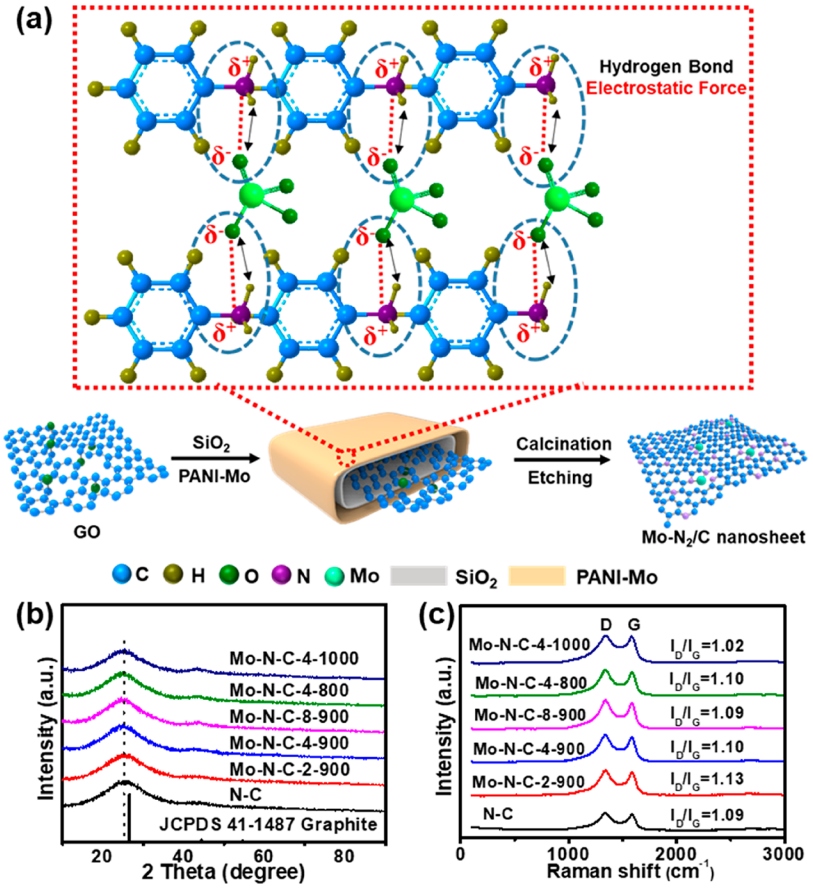

Figure 1. (a) The schematic illustration of the preparation of Mo−N−C nanosheets. (b) XRD patterns and (c) Raman spectra of the studied Mo−N−C and N−C samples.

that damages the cycling performance and decreases the columbic efficiency.[18−21]

Nanostructured carbon materials have been widely used to improve the electron conductivity of S, while the confinement of LiPS is still challenging due to the poor affinity of nonpolar neat carbon with LiPS. Doping carbon with heteroatoms (N, P, O, *etc.*) can improve the interaction between carbon substrates and LiPS, while the long-term cycling performance is still unsatisfactory. Transition-metal oxides (*e.g.*, MnO_2,[22] Ti_4O_7,[23] SnO_2,[24] Co_3O_4[20]), metal sulfides (*e.g.*, ZnS,[25] WS_2[26]), or metal phosphides (*e.g.*, CoP,[27] Ru-doped Mo_4P_3[28]) with inherent polarity can deliver stronger affinity with LiPS than carbon and improve the kinetics of the LiPS conversion to a certain degree. Recently, metal−nitrogen−carbon (M−N−C) materials such as Fe−N−C,[29−31] Co−N−C,[32,33] and Ni−N−C[34] have demonstrated encouraging performance as Li−S battery cathodes due to their M−N_x/C active sites and highly porous structures. However, it is still exceptionally challenging to improve their intrinsic activity toward LiPS conversion and the cycling performance in Li−S battery. This may be attributed to the relatively weak adsorption capability toward LiPS and low surface areas of the reported M−N−C materials, failing to endow efficient LiPS conversion in long-term cycling. In biomimetic catalysis studies, molybdoenzymes with monatomic molybdenum (Mo) sites, such as nitrogenase and xanthine oxidase, have been regarded as effective catalysts for N_2 fixation and xanthine oxidation.[35,36] In these enzymes, each Mo atom is 3-fold coordinated with S ligands to form triple Mo−S bonds, which act as the active centers to receive the hydrogen transferred from reactants. When contacting with LiPS, metallic Mo can also form stable Mo−S chemical bonding with a large formation energy of 2.6 eV.[37] Inspired by these studies, it is potentially promising to design a Mo−N−C electrode with monatomic Mo centers toward rapid LiPS catalytic conversion for a high-performance Li−S battery.

In this study, Mo−N−C nanosheets with atomically dispersed Mo−N_2/C active sites are developed and employed as bifunctional catalysts toward Li_2S deposition/decomposition in a Li−S battery. The Mo−N coordination configuration and high surface area/pore volume of Mo−N−C provide high activity for LiPS catalytic conversion and sufficient entrapment of LiPS, which effectively suppress the shuttle effect. As a result, even under a 5 C rate in a Li−S battery, the S/Mo−N−C composite electrode still delivers a high reversible capacity of 743.9 mAh g^{-1}. Meanwhile, the S/Mo−N−C with a high S content of 81% show a reversible capacity of 890.7 mAh g^{-1} after 550 cycles under 2 C rate with an insignificant capacity decay of 0.018% per cycle. Theoretical calculations indicate the Mo−N_2/C structure can bifunctionally lower the energy barriers of Li_2S deposition and decomposition, thereby facilitating the kinetics of the LiPS catalytic transformation and ensuring an excellent rate and cycling performance in the Li−S battery.

RESULTS AND DISCUSSION

The preparation procedure of Mo−N−C nanosheets is illustrated in Figure 1a which involves the *in situ* growth

https://dx.doi.org/10.1021/acsnano.0c03325
ACS Nano 2020, 14, 10115−10126

and polymerization of aniline, Mo, and silica precursors onto graphene oxide (GO) and subsequent annealing and etching processes (details see Experimental Section). Here, GO acts as the template for catalyst preparation, which is converted to reduced graphene oxide (rGO) during reductive annealing to improve the electric conductivity of Mo−N−C. The silica was prepared by the hydrolysis of tetraethyl orthosilicate (TEOS) and employed to protect the Mo−N−C nanosheets against aggregation during high-temperature annealing. The PANI could act as both the nitrogen source and the chelating agent to coordinate with metal ions.[38,39] In our case, the negatively charged MoO_4^{2-} anions from ammonium heptamolybdate (AHM) could strongly interact with *in situ* generated PANI (with aniline/Mo molar ratio of 4/1) through electrostatic forces and hydrogen bonds.[40−42] The resulted PANI-Mo composite could effectively stabilize Mo atoms against agglomeration during high-temperature pyrolysis at 900 °C and produce Mo−N−C nanosheets with atomically dispersed Mo−N_x/C sites (denoted as Mo−N−C-4-900). For comparison, the Mo−N−C-4-900 samples with different aniline/Mo ratios (2:1 and 8:1, denoted as Mo−N−C-2-900 and Mo−N−C-8-900, respectively), pyrolysis temperatures (800 and 1000 °C, denoted as Mo−N−C-4-800 and Mo−N−C-4-1000, respectively), the sample without the addition of Mo (denoted as N−C) and the Co−N−C and Fe−N−C samples with similar synthetic method to Mo−N−C were also prepared.

The crystal phases of the synthesized Mo−N−C and N−C samples are observed by X-ray diffraction (XRD) (Figure 1b). The diffraction peaks at 25.1° and 43.3° are indexed to (002) and (101) planes of graphite (JCPDS 41-1487), respectively. Notably, no Mo-related peaks can be observed in the XRD patterns of the studied samples, suggesting the high dispersity of Mo atoms after acid etching. The leached species of Mo−N−C-4-900 are confirmed to be Mo_2C (JCPDS 35-0787) according to the XRD pattern (Figure S1a) and high-resolution transmission electron microscope (HRTEM) image (Figure S1b). The carbon structures of the studied samples are further probed by Raman spectroscopy (Figure 1c). The obviously lower intensity ratio of D peak to G peak (I_D/I_G) of Mo−N−C-4-1000 than that of other Mo−N−C and N−C samples demonstrates a lower degree of carbon structure disordering when annealed at 1000 °C. Besides, it is found that the disordering degree of carbon can be regulated by controlling the Mo content in Mo−N−C, as Mo−N−C-2-900 has a higher I_D/I_G value than that of Mo−N−C-4-900, Mo−N−C-8-900, and N−C.

Both Mo−N−C-4-900 and N−C reveal the nanosheet morphology in the scanning electron microscope (SEM) images (Figures S2a and S3). Most of the Mo−N−C-4-900 nanosheets are separated with each other, as observed in the low-magnification SEM image (Figure S2b). As displayed in the TEM image of Mo−N−C-4-900 (Figure 2a), no Mo-relating nanocrystals can be found, and nanopores with diameters of 10−20 nm can be clearly observed. The highly porous Mo−N−C-4-900 sample exhibits an enhanced Brunauer−Emmett−Teller (BET) total surface area of 1038 $m^2\ g^{-1}$ and a meso-/macropore surface area of 732 $m^2\ g^{-1}$ (Figures S4−S5) compared to N−C (427 $m^2\ g^{-1}$ for total and 312 $m^2\ g^{-1}$ for meso-/macropores), suggesting the critical role of Mo in catalyzing the formation of defect-rich nitrogen-doped carbon.[39,43] Atomic-resolution aberration corrected high-angle annular dark-field scanning TEM (HAADF-STEM) measurement (Figure 2b) demonstrates that Mo

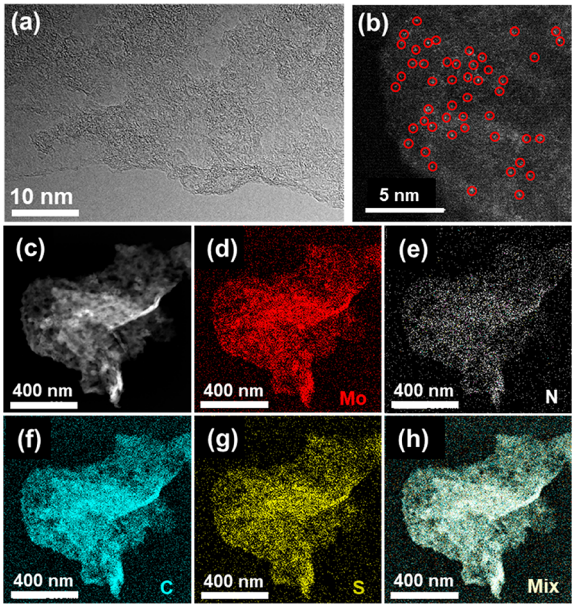

Figure 2. (a) TEM image of Mo−N−C-4-900, (b) the atomic STEM image of Mo−N−C-4-900, (c) HAADF-STEM image of S/Mo−N−C-4-900, and (d−h) the corresponding elemental mapping image of S/Mo−N−C-4-900 (red for Mo (d), white for N (e), blue for C (f), yellow for S (g)).

atoms are atomically dispersed throughout the nitrogen-doped carbon sheet in Mo−N−C-4-900. Elemental analysis by the X-ray photoelectron spectroscopy (XPS) (Table S1) shows that the surface content of Mo in Mo−N−C-4-900 is *ca.* 0.36 at%. In order to investigate the elemental distribution, the energy dispersive spectrometer (EDS) elemental mapping tests were further conducted on Mo−N−C-4-900 before (Figure S6) and after S infiltration (Figure 2c−h). The results reveal that the Mo, N, C, and S are homogeneously distributed throughout the nanosheet. The morphologies of Mo−N−C-8-900, Mo−N−C-2-900, Mo−N−C-4-800, and Mo−N−C-4-1000 are also analyzed (Figures S7−S10). Mo−N−C-8-900 with a higher aniline/Mo ratio exhibits a similar morphology with Mo−N−C-4-900 but a smaller surface area (655 $m^2\ g^{-1}$) and Mo content (0.25 at%). When reducing the aniline/Mo ratio during the synthesis, Mo−N−C-2-900 delivers a further decreased surface area of 587 $m^2\ g^{-1}$ but a much enhanced Mo content (0.93 at%), which can be attributed to the presence of aggregated Mo_2C nanoparticles (Figure S8). Changing the pyrolysis temperature would not affect the nanosheet morphology much (Figures S9 and S10) but lead to smaller surface areas relative to Mo−N−C-4-900 (529 $m^2\ g^{-1}$ for Mo−N−C-4-800 and 561 $m^2\ g^{-1}$ for Mo−N−C-4-1000). Besides the total surface area, it is found that the Mo−N−C-4-900 (732 $m^2\ g^{-1}$) shows a higher surface area of meso-/macropore than that of Mo−N−C-4-800 (264 $m^2\ g^{-1}$), revealing that 800 °C is insufficient for Mo−N−C to form a large amount of meso-/macropores during the annealing process. The pore volume distributions of the studied Mo−N−C samples are presented in Figure S11. When the pyrolysis temperature increases, Mo−N−C-4-1000 exhibits a higher portion of macropores but a lower portion of micro/mesopores compared to Mo−N−C-4-900. Although Mo−N−C-4-1000 nanosheets seem rougher than Mo−N−C-900 (Figure S9), the change of pore structure leads to a lower

https://dx.doi.org/10.1021/acsnano.0c03325
ACS Nano 2020, 14, 10115−10126

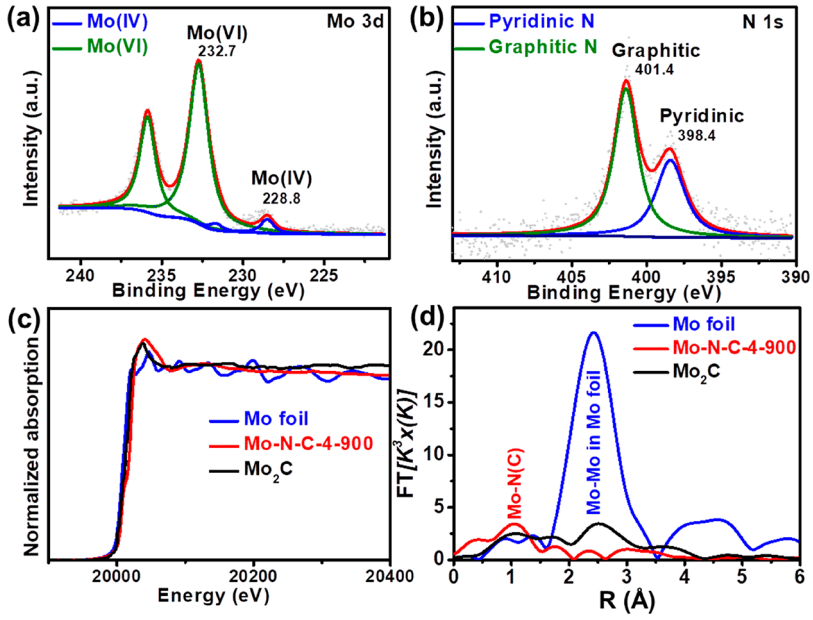

Figure 3. High-resolution (a) Mo 3d and (b) N 1s XPS spectra of Mo−N−C-4-900. Mo K-edge (c) XANES and (d) k^3-weighted FT-EXAFS spectra of Mo−N−C-4-900, Mo foil, and Mo_2C samples.

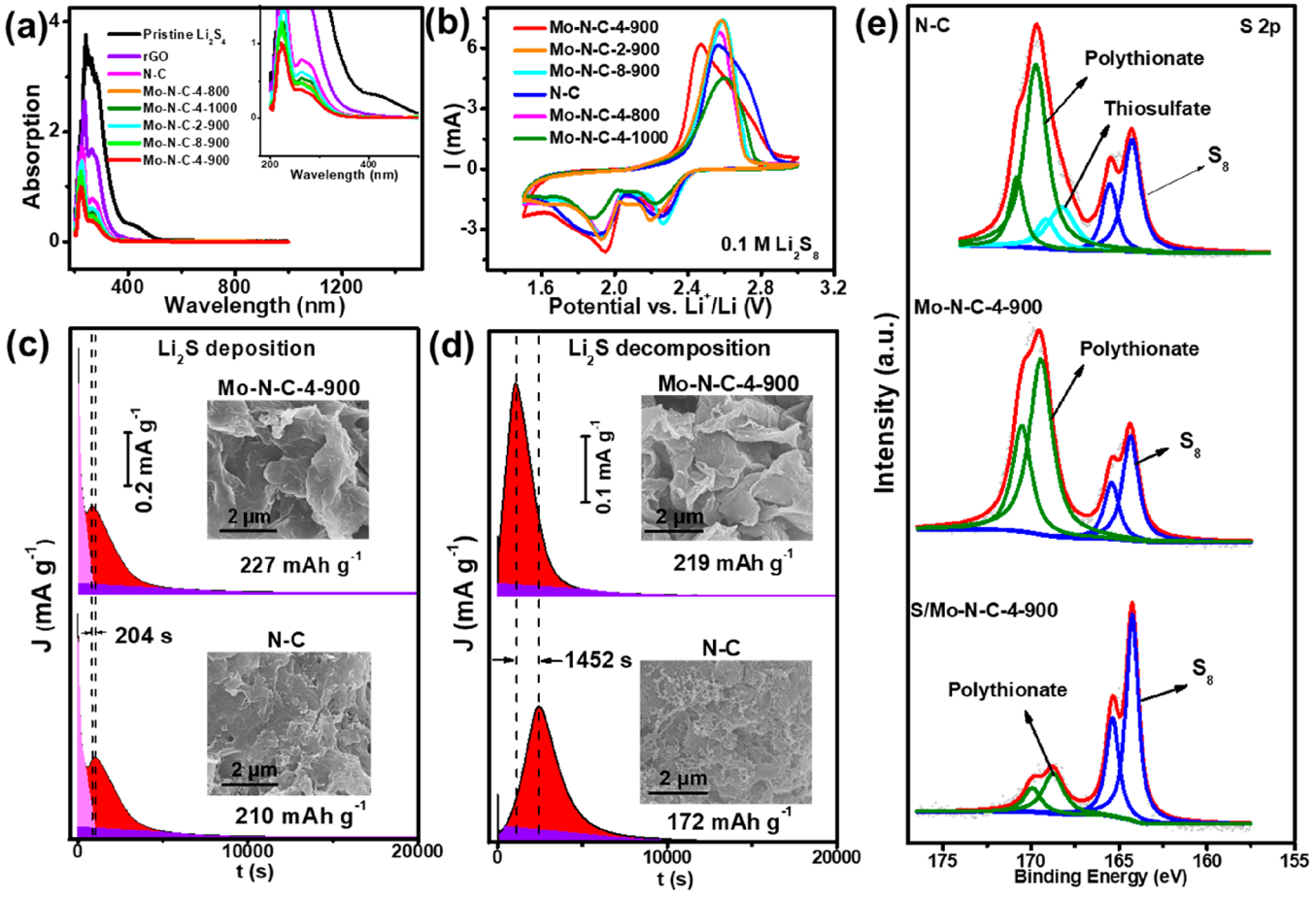

Figure 4. (a) UV−vis spectra of the Li_2S_4 solution after immersion with the studied samples. (b) LiPS conversion experiment of the electrodes measured in 0.1 M Li_2S_8 catholyte, scan rate: 1 mV s^{-1}. Li_2S (c) deposition and (d) decomposition tests on Mo−N−C-4-900 and N−C. The red areas represent the amount of Li_2S deposited or decomposed. The insets of (c) and (d) show the morphologies of electrodes after the tests. (f) S 2p XPS spectra of N−C, Mo−N−C-4-900 electrode after Li_2S decomposition measurement, and the as-prepared S/Mo−N−C-4-900 electrode.

https://dx.doi.org/10.1021/acsnano.0c03325
ACS Nano 2020, 14, 10115−10126

total surface area of Mo−N−C-4-1000 than that of Mo−N−C-4-900.

After S infiltration, the obtained S/Mo−N−C-4-900 maintains the nanoplate morphology (Figure S12) and homogeneous distribution of Mo, N, C, and S (Figure 2c−h), representing the full incorporation of S into the Mo−N−C even though some of the Mo−N−C-4-900 nanosheets are compacted. The S contents of S/Mo−N−C-4-900 and S/N−C (as a reference) are measured to be 81.0 and 80.8 wt % by the thermogravimetric analysis (TGA) (Figure S13), respectively.

XPS measurement was employed to detect the valence state of Mo in the Mo−N−C samples (Figure 3a). The high-resolution Mo 3d spectrum of Mo−N−C-4-900 can be deconvoluted into two pairs of peaks. One pair located at 228.8 and 231.9 eV can be assigned to $3d_{3/2}$ and $3d_{5/2}$ peaks of Mo(IV), and the other one at 233.2 and 236.7 eV is responsible for the Mo(VI).[44,45] The ratio of Mo(IV) to Mo(VI) is calculated to be 1:17, suggesting the dominant oxidation state of the Mo atom in Mo−N−C-4-900 is +6. In the high-resolution N 1s spectrum (Figure 3b), two peaks at 398.4 and 401.4 eV represent pyridinic and graphitic N, respectively.[29,32,46] Of them, only pyridinic N located in the edge of carbon plane could coordinate with Mo to form Mo−N_x/C sites.[47] In addition, the nitrogen doping into carbon material could improve the affinity and interaction of carbon with LiPS and inhibit the migration of LiPS.[32−34,48] To investigate the valence state and local coordination structure of the Mo−N−C-4-900 sample, X-ray photoelectron spectroscopy (XAS) measurements were carried out. The Mo K-edge X-ray absorption near-edge structure (XANES) of Mo−N−C-4-900 is shown in Figure 3c. Compared to Mo foil and Mo_2C references, the adsorption edge of Mo in Mo−N−C-4-900 exhibits a slightly positive shift, indicating that the average valence of the Mo in Mo−N−C-4-900 is higher than +2. Figure 3d displays the k^3-weighted Flourier transformed extended X-ray absorption fine structure (FT-EXAFS) spectra of Mo−N−C-4-900, Mo_2C, and Mo foil samples. The major peak of Mo−N−C-4-900 sample at 1.1 Å represents the Mo−N(C) coordination (Figure 3d),[40,47,49] and the peak corresponding to Mo−Mo coordination at 2.4 Å is very weak, representing that most of the Mo atoms in Mo−N−C-4-900 are atomically dispersed and coordinated with N(C). The EXAFS fitting curves (Figure S14) and fitting results (Table S2) indicate that the single Mo atom exhibits a coordination number (CN) of ∼2.25 with N(C) and a mean Mo−N bond distance of 1.440 Å. As the Mo−N bond is slightly shorter than Mo−C,[47] the location of the FT amplitude near 1.1 Å of Mo−N−C-4-900 shifts slightly to the negative direction compared with that of Mo_2C. Considering the possible oxidation of Mo during *ex situ* XAS, the practical CN of Mo−N in Mo−N−C-4-900 should be close to 2, revealing the formation of the Mo−N_2/C active center.

The ultraviolet−visible (UV−vis) spectrum measurements were performed to study the adsorption capability of the studied samples with LiPS. As is shown in Figure 4a, the Mo−N−C-4-900 exhibits the lowest adsorption peak among the studied samples, and all the Mo containing samples show superior adsorption capability to N−C and rGO.

The kinetics of LiPS electrocatalytic conversion is evaluated by the cyclic voltammetry (CV) measurement (Figure 4b) with a scan rate of 1 mV s^{-1} in asymmetric battery as reported before.[20] The Mo−N−C-4-900 asymmetric cell shows an onset potential of 2.46 V in the reduction process and two cathodic peaks at 2.25 and 1.95 V which represent the reduction of Li_2S_8 to Li_2S_4 and Li_2S_4 to Li_2S, respectively. Compared to Mo−N−C-4-900, the N−C electrode delivers a slightly lower onset potential of 2.44 V for the first cathodic peak, indicating the high intrinsic activity of Mo−N−C-4-900 in Li_2S_8 reduction. While it can be observed that the second cathodic peak (1.90 V) of N−C relating to the reduction of Li_2S_4 to Li_2S is obviously lower than that of Mo−N−C-4-900. This demonstrates that the Mo−N−C-4-900 mainly accelerates the conversion of Li_2S_4 to Li_2S process of LiPS electrocatalytic conversion. This result is also proved by the Li_2S deposition measurement (Figure 4c) in which the Mo−N−C-4-900 and N−C asymmetric batteries were subject first to a discharge process under constant current of 0.1 mA until the potential approaches 2.05 V and then held at 2.05 V. The current was recorded to evaluate the Li_2S nucleation capability on the catalysts. As studied before,[50,51] the time when the maximum current density occurs can reflect the catalytic activity of the catalysts in Li_2S deposition/decomposition. It can be observed from the *I*−*t* curves (Figure 4c) that the peak position of Mo−N−C-4-900 (862 s) is obviously earlier than the N−C (1066 s), pointing to enhanced Li_2S deposition kinetics on Mo−N−C-4-900. As for the anodic process, the Mo−N−C-4-900 delivers a much superior activity in Li_2S decomposition (onset potential of 2.05 V) and peak potential (2.46 V) to N−C (onset potential of 2.1 V and peak potential of 2.56 V) and other Mo−N−C control electrodes (Figure 4b). The Li_2S decomposition measurement with a constant potential of 2.3 V (Figure 4d) after the Li_2S deposition indicates a much earlier and larger peak of Mo−N−C-4-900 (1040 s) than N−C (2492 s) and a higher amount of Li_2S decomposed on Mo−N−C-4-900 (corresponding to 219 mAh g^{-1}) than N−C (172 mAh g^{-1}), representing the enhanced Li_2S oxidation kinetics on Mo−N_2/C sites.

The asymmetric batteries of Mo−N−C-4-900 and N−C were disassembled and subjected to SEM and XPS measurements. Obviously, many nanoparticles can be observed on N−C electrode after Li_2S decomposition (the inset of Figure 4d) process when compared with the initial N−C electrode (Figure S15d). These nanoparticles are proved to be S relating species according to the EDS spectra (Figure S16), revealing the incomplete decomposition of Li_2S on N−C surface. In a sharp contrast, the Mo−N−C-4-900 electrode (the inset of Figure 4d and Figures S15 and S17) after Li_2S decomposition measurement delivers similar morphology with the pristine one (Figure S15a). Given that the Mo 3d XPS spectrum of the Mo−N−C-4-900 electrode after Li_2S decomposition (Figure S18) is very similar to that before the tests, it is assumed that the majority of the Mo atoms in Mo−N−C-4-900 is still in +6 oxidation state, suggesting a high stability of Mo−N−C-4-900 during the Li_2S deposition/decomposition processes. After Li_2S decomposition, the S 2p spectra of both N−C (Figure 4e, up) and Mo−N−C-4-900 (Figure 4e, middle) electrodes show two pairs of peaks at 162.8/164.1 eV and 169.3/170.5 eV. The latter one may be related to the partial oxidation of S species when exposed in air, which can be observed in all the studied electrodes and even the fresh S/Mo−N−C-4-900 electrode (Figure 4e, down). The peaks at 162.8/164.1 eV can be assigned as the S_8, considering the similar peaks in the S 2p spectrum of fresh S/Mo−N−C-4-900. It should be noted that a pair of peaks at 167.9/168.9 eV

https://dx.doi.org/10.1021/acsnano.0c03325
ACS Nano 2020, 14, 10115−10126

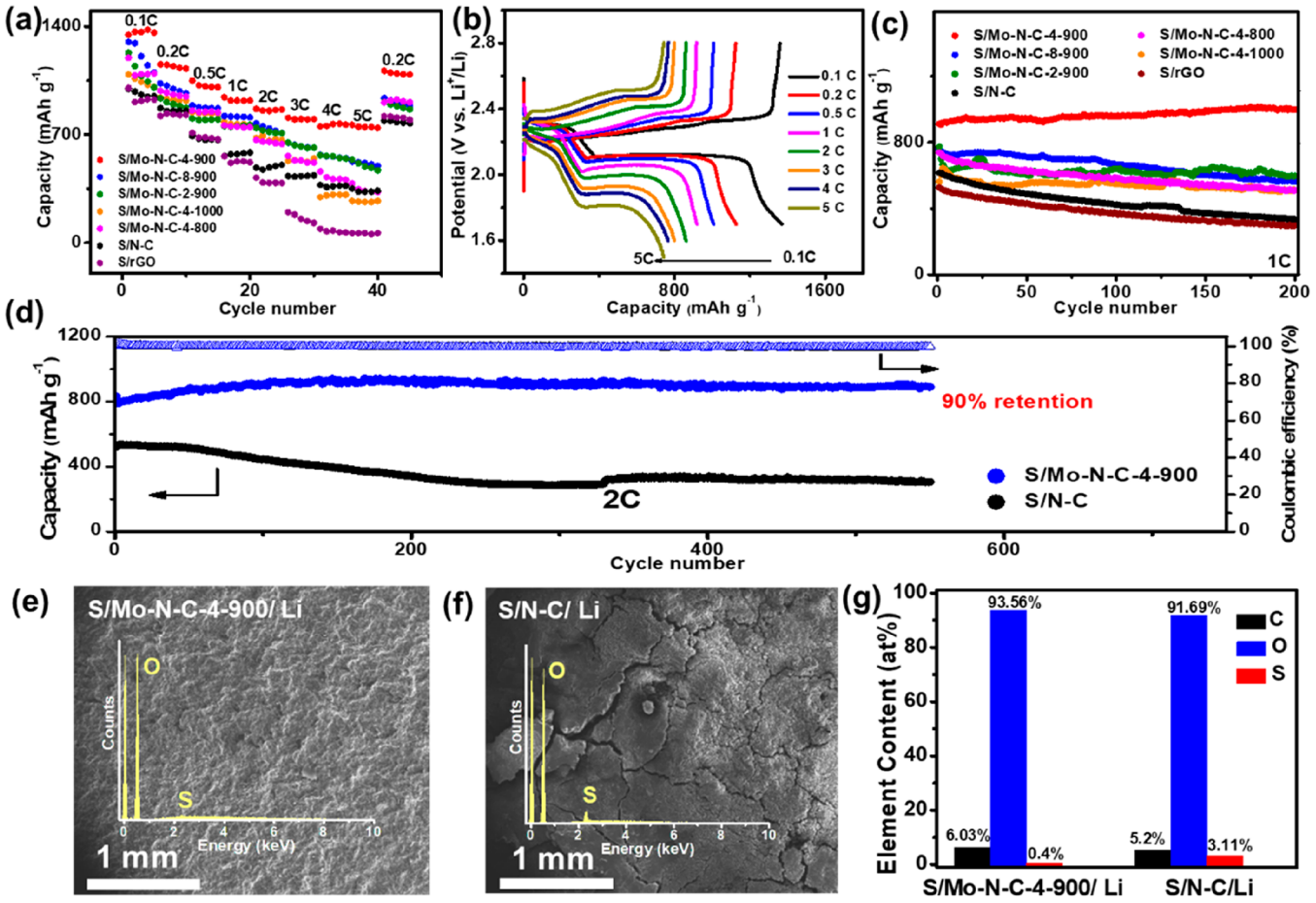

Figure 5. (a) Rate performance of the studied electrodes. (b) Discharge/charge profiles of S/Mo−N−C-4-900 under various current densities. (c) Cycling performance of the electrodes at 1 C rate. (d) Cycling performance of S/Mo−N−C-4-900 and S/N−C electrodes at 2 C rate. The SEM images of the cycled Li anodes with (e) S/Mo−N−C-4-900 and (f) S/N−C as cathodes. (g) The elemental contents of the cycled Li anodes. The inserts of (e) and (f) present the EDS spectra of the cycled Li anodes. The signal of Li cannot be detected in the EDS measurement.

can be deconvoluted in the S 2p spectrum of N−C, likely attributing to the thiosulfate[40] derived from the incomplete oxidation of Li_2S.

To demonstrate the performance of the developed Mo−N−C electrodes in Li−S battery, the rate performance of S/Mo−N−C-4-900 and other control samples is displayed in Figure 5a. The reversible capacity of S/Mo−N−C-4-900 (1360.2 mAh g^{-1}) at 0.1 C rate is obviously higher than the other electrodes (*e.g.*, 950.2 mAh g^{-1} for S/N−C, 1101.8 mAh g^{-1} for S/Mo−N−C-8-900, and 926.4 mAh g^{-1} for S/rGO). After increasing the current density to 0.2, 0.5, 1, 2, 3, 4, and 5 C, S/Mo−N−C-4-900 still reaches high reversible capacities of 1128.1, 1007.3, 919.8, 862.2, 799.4, 765.2, and 743.9 mAh g^{-1}, respectively. As for S/Mo−N−C-8-900 with a lower Mo content, it delivers a high initial capacity of 1300.0 mAh g^{-1} at 0.1 C but quickly decreases to 1101.0 mAh g^{-1}. The rapid capacity decay in the initial several cycles may result from the lower Mo content and degree of carbon structure disordering of Mo−N−C-8-900 which fails to provide adequate amounts of Mo−N_x site for LiPS anchoring. When conducted at 3 C, S/Mo−N−C-8-900 exhibits a capacity of 618.1 mAh g^{-1}, obviously lower than that of S/Mo−N−C-4-900. Similarly, S/Mo−N−C-2-900 with a higher total Mo content delivers a lower capacity of 614.2 mAh g^{-1} at 3 C relative to that of S/Mo−N−C-4-900, most likely due to the blockage of Mo−N_x/C sites by the existence of Mo_2C particles. Additionally, it is found that the capacity retention under high current density is strongly dependent on the pyrolysis temperature of the Mo−N−C samples. Both S/Mo−N−C-4-800 and Mo−N−C-4-1000 display reduced capacities at the 3 C rate compared to that of S/Mo−N−C-4-900 (562.0 mAh g^{-1} and 533.0 mAh g^{-1}, respectively). As a comparison, the S/N−C and S/rGO electrodes exhibit initial capacities of 994 and 1001 mAh g^{-1} at 0.1 C and deliver 435.0 and 128.0 mAh g^{-1} at 3 C, respectively. Meanwhile, the capacity and the rate performance of Co−N−C and Fe−N−C samples are also investigated. As shown in Figure S19, the S/Co−N−C and S/Fe−N−C cathodes exhibit the initial capacities of 1256.6 and 1176.8 mAh g^{-1} and retain 363.8 and 342.5 mAh g^{-1} at 5 C rate, respectively, both of which are lower than that of S/Mo−N−C-4-900. The significantly suppressed capacity and rate performance of the electrodes in the absence of Mo metal demonstrate the critical role of Mo−N_2/C sites on the electrochemical performance enhancement.

The corresponding potential−capacity curves of all the studied electrodes under different current densities are displayed in Figure 5b and Figure S20. The discharge profile of S/Mo−N−C-4-900 at 0.1 C consists of a high short plateau at 2.35 V and a long plateau at 2.12 V which refer to the reduction of S_8 to Li_2S_4 and the further transformation of

https://dx.doi.org/10.1021/acsnano.0c03325
ACS Nano 2020, 14, 10115−10126

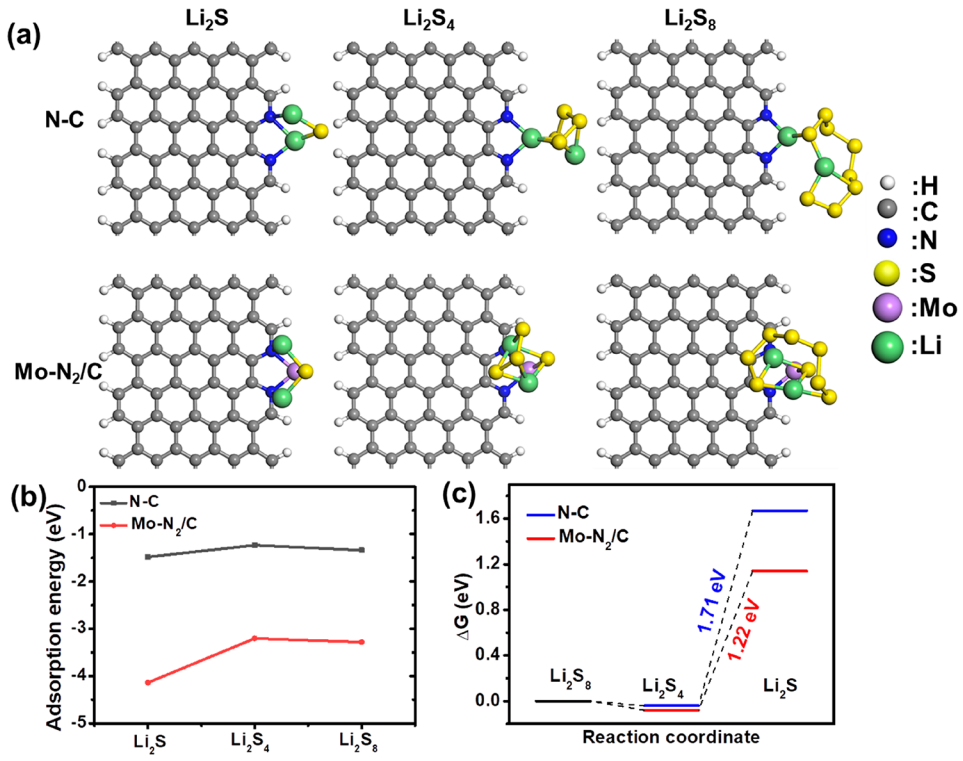

Figure 6. (a) The optimized adsorption conformations of LiPS on N−C and Mo−N_2/C. (b) Adsorption energies of Mo−N_2/C and N−C for Li_2S_8, Li_2S_4, and Li_2S. (c) Gibbs free energy changes of Li_2S_8, Li_2S_4, and Li_2S on Mo−N_2/C and N−C.

Li_2S_4 to Li_2S. As for the charge profile of S/Mo−N−C-4-900 at 0.1 C, a long inclined plateau in the range of 2.2−2.3 V and a short plateau at 2.31 V are presented, corresponding to the Li_2S decomposition and LiPS oxidation.[20,28] Even under 5 C rate, S/Mo−N−C-4-900 still exhibits two distinctive plateaus at 2.13 and 1.82 V in discharge profile. Although the S/N−C electrode exhibits two similar plateaus to S/Mo−N−C-4-900 at 2.30 and 2.12 V in discharge profile at 0.1 C, it delivers negligible capacity in the second discharge plateau when conducted at 5 C (Figure S20a), indicating a large polarization and poor Li_2S deposition kinetics under high current density.

The electrochemical impedance spectroscopy (EIS) curves of the studied electrodes are presented in Figure S21. The semicircles at high- and medium-frequency regions refer to the charge-transfer resistance (R_{ct}) and the sloping line in the low-frequency region corresponds to the diffusion of Li ion.[52,53] It can be observed that all of the Mo−N−C electrodes show a smaller R_{ct} than S/N−C and S/rGO.

When repeating discharge/charge cycles at 1 C rate (Figure 5c), the S/Mo−N−C-4-900 electrode exhibits an initial capacity of 912.0 mAh g^{-1} and shows no capacity decay after 200 cycles. In the contrast, the S/N−C remains only 54% capacity after 200 cycles. As for the other electrodes, they also show obvious capacity deterioration after cycling (*e.g.*, 25% loss for S/Mo−N−C-8-900 and 30% loss for S/Mo−N−C-4-800). The prolonged cycling stability results of S/Mo−N−C-4-900 and S/N−C under 2 C rate are also given (Figure 5d). The S/Mo−N−C-4-900 delivers a high capacity of 831.0 mAh g^{-1} in the beginning. The capacity gradually increases in the initial 100 cycles, possibly due to the activation of S,[52−54] and reaches the highest value of 908.0 mAh g^{-1}. After 550 discharge/charge repeating cycles, it still holds a capacity retention of 90% and an exceptionally low capacity decay rate of 0.018% per cycle, outperforming most of the previously reported results (Table S3). The Coulombic efficiency of S/Mo−N−C-4-900 in a long-term cycling is higher than 99%, indicating a high reversibility as well as stability. In contrast, the S/N−C electrode reveals a severe capacity decay with a much lower capacity of 303.8 mAh g^{-1} after cycling. The enhancement in cycling stability of S/Mo−N−C-4-900 is based on the fact that the dissolution and diffusion of LiPS are alleviated as the Li_2S deposition/decomposition processes are propelled on Mo−N−C-4-900. The morphologies of S/Mo−N−C-4-900 and S/N−C after cycling were observed by SEM measurements (Figure S22). The S/Mo−N−C-4-900 electrode after cycling still maintains the nanosheet morphology (Figure S23b). However, S/N−C is fully covered by the deposited S after cycling (Figure S22c,d), revealing its weak adsorption ability and low intrinsic activity for LiPS conversion. After cycling, the EIS plots of S/Mo−N−C and S/N−C are composed of two semicircles (Figure S24), which correspond to the passivation layer on the electrode derived from the deposited S species and R_{ct}, respectively. The smaller resistance of cathodic passivation layer on S/Mo−N−C-4-90 compared to S/N−C indicates the suppressed accumulation and facilitated kinetics of LiPS.

Since $LiNO_3$ was widely used as an additive in electrolytes to alleviate the shuttle effect, the electrochemical performance of S/Mo−N−C-4-900 and S/N−C in Li−S batteries with $LiNO_3$-free electrolytes was further evaluated. As shown in Figure S25, the initial discharge capacity of S/N−C is only 853.2 mAh g^{-1}, and a large overcharge can be observed (5086.0 mAh g^{-1} in the first cycle). However, the S/Mo−N−C-4-900 shows much a depressed overcharge and a much higher discharge capacity (1110.1 mAh g^{-1}) compared to S/N−C. This result confirms the diffusion loss of S species in

https://dx.doi.org/10.1021/acsnano.0c03325
ACS Nano 2020, 14, 10115−10126

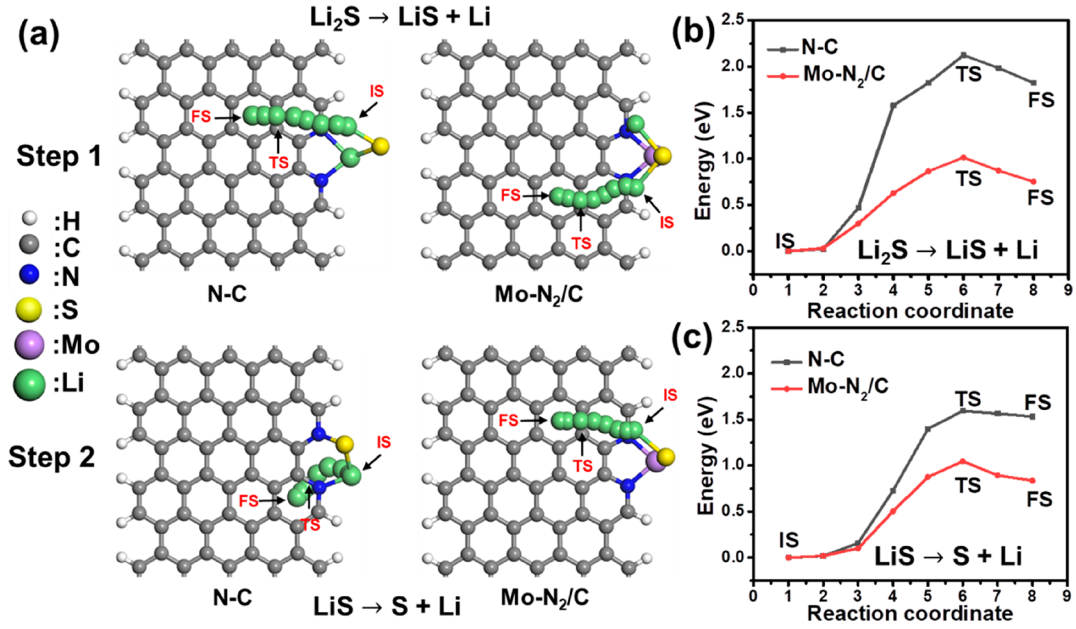

Figure 7. (a) Decomposition pathways of Li_2S to LiS and LiS to S on Mo−N_2/C and N−C. (b) and (c) Energy profiles for the decomposition of Li_2S on Mo−N_2/C and N−C in step 1 (b) and step 2 (c). The IS, TS, and FS represent the initial state, transition state, and final state, respectively, along the decomposition pathway of Li_2S.

the discharge/charge process can be alleviated on Mo−N−C-4-900.

As the LiPS migration can induce several detrimental side reactions and the consequent corrosion of Li anodes,[50] the morphology and S contents of Li anodes after cycling were characterized by SEM and EDS measurements. As shown in Figure 5e,f, the Li anode of S/N−C shows obvious cracks resulting probably from the corrosion of LiPS and strong signal of S element (3.11 at%). On the contrary to S/N−C, the anode of S/Mo−N−C-4-900 exhibits a smoother surface and lower S signal in EDS spectrum (0.4 at%), revealing a reduced anode corrosion (Figure 5g). The lower S content on anode side demonstrates the successful suppression of a shuttle effect in the S/Mo−N−C-4-900 battery that enlarges the lifespan of the Li−S battery.

In order to implement the developed S/Mo−N−C-4-900 in the practical Li−S battery, it is vital to increase the S loading of the cathode. With this in mind, S/Mo−N−C-4-900 with a high S loading of 8.0 mg cm^{-2} was prepared and its cycling performance under 0.1 C rate is given in Figure S26. The S/Mo−N−C-4-900 delivers a reversible areal capacity of 8.6 mAh cm^{-2} initially and 7.5 mAhcm^{-2} after 70 cycles at 0.1 C, still much higher than that of commercial LIB (4.0 mAh cm^{-2}). This respectable areal capacity and capacity retention (87%) of S/Mo−N−C-4-900 may benefit from the intrinsically high activity of Mo−N−C-4-900 for LiPS conversion and the alleviated shuttle effect.

Density functional theory (DFT) calculations were performed to elucidate the mechanism that the Mo−N_2/C structure promotes the transformation of LiPS. The local structure and the optimized adsorption conformation of LiPS on N−C and Mo−N_2/C are displayed in Figure S27 and Figure 6a, respectively. Obviously, the adsorption energies of Li_2S_8, Li_2S_4, and Li_2S on Mo−N_2/C are higher than the adsorption energy on N−C (Figure 6b). The higher adsorption energy brings about an enhanced adsorption capability of Mo−N_2/C for LiPS entrapment, consistent with the UV−vis results. The Gibbs free energies of Li_2S_8, Li_2S_4 and Li_2S on Mo−N_2/C and N−C surfaces are also calculated (Figure 6c). As is shown, Mo−N_2/C shows small and similar Gibbs free energy change (ΔG) in the Li_2S_8/Li_2S_4 conversion to N−C. The Li_2S_4/Li_2S conversion is found to be the rate-determining step of Li_2S deposition on both systems, and the ΔG of Li_2S_4/Li_2S conversion on Mo−N_2/C (1.22 eV) is significantly lower than that on N−C (1.71 eV). The smaller ΔG suggests that the activation energy of Li_2S nucleation is lowered in Mo−N_2/C.

We calculate the decomposition barrier of Li_2S in the charging process of Li−S battery. The decomposition of Li_2S includes an initial delithiation of Li_2S to yield LiS and further delithiation of LiS to generate S (Figure 7a). Mo−N_2/C delivers decomposition barriers of 1.01 and 1.04 eV for Li_2S/LiS and LiS/S transformations (Figure 7b,c), respectively, both of which are lower than that of N−C (2.12 and 1.59 eV). The lowered decomposition barriers in Mo−N_2/C can substantially enhance the delithiation kinetics of Li_2S and increase the reversibility of LiPS transformation, both confirmed by the electrochemical decomposition tests of Li_2S.

CONCLUSION

In summary, porous Mo−N−C nanosheets with atomically dispersed Mo−N_2/C active sites were developed and employed as an efficient and durable cathode for Li−S battery. The Mo−N coordination structure as well as the high surface area of Mo−N−C nanosheets lead to high LiPS adsorption ability and efficient suppression against the shuttle effect. As a result, the S/Mo−N−C battery delivers a high capacity of 743.9 mAh g^{-1} under 5 C and is quite stable in long-term cycling with a very low capacity decay rate of 0.018% per cycle over 550 cycles at 2 C rate. Even with a high S loading of 8.0 mg cm^{-2}, the S/Mo−N−C displays an areal capacity of 8.6 mAh cm^{-2} at 0.1 C in the beginning and 7.5 mAh cm^{-2} after 70 cycles, holding promise in the implementation of practical Li−S batteries. DFT calculations

https://dx.doi.org/10.1021/acsnano.0c03325
ACS Nano 2020, 14, 10115−10126

demonstrate that the Mo−N_2/C structure can bifunctionally reduce the energy barriers for Li_2S deposition and decomposition, resulting in enhanced LiPS transformation kinetics and excellent rate capability/stability in the Li−S battery. This work presents a strategy on developing rationally designed catalysts for practical Li−S batteries and other energy conversion/storage devices.

EXPERIMENTAL SECTION

Chemicals and Materials. Flake graphite was obtained from Nanjing XFNANO Materials Tech Co., Ltd. $NaNO_3$, $KMnO_4$, H_2O_2 (30 wt %), polyvinylpyrrolidone (PVP, K27), tetraethyl orthosilicate (TEOS), concentrated ammonia solution (25%), ammonium molybdate (AHM), NaOH, $LiNO_3$, and aniline were purchased from Aladdin. Lithium bis-trifluoromethanesulfonimide (LiTFSI), 1,2-dimethoxyethane (DME), and 1,3-dioxolane (DOL) were purchased from Sigma-Aldrich.

Material Synthesis. *Preparation of Graphene Oxide.* GO was prepared by a modified Hummers method reported before.[55] Briefly, 50 mL of concentrated sulfuric acid was slowly added into the mixture of 2 g of flake graphite and 0.5 g of $NaNO_3$ with gentle stirring. The suspension was kept stirring under ice-bath condition for 2 h. After that, 7 g of $KMnO_4$ was slowly added into it to form a green-colored thick paste. After continuous stirring for 2 h, 200 mL of water and 5 mL of H_2O_2 (30 wt %) were consequently dropped into the paste. The color of the formed suspension turned yellow. The suspension was subjected to a hot HCl solution (5 wt %) and deionized water washing until the pH value was higher than 6 and then redispersed in deionized water under sonication to form a uniform suspension of GO with a concentration of 3 mg mL^{-1}.

Preparation of Mo−N−C-4-900. Six mL of GO solution (3 mg mL^{-1}) was added to 44 mL of water and 350 mL of ethanol solution with a stirring speed of 500 rpm. After that 0.6 g of PVP (K27), 14 mL of TEOS, and 11 mL of concentrated ammonia solution were introduced in sequence to form a transparent brown solution. After stirring for 12 h, the transparent solution turned to a suspension with maize color which was centrifuged and washed with deionized water for 2 times and redispersed in 300 mL of deionized water. Then 4 mL of concentrated HCl and 4 mL of aniline were added to the obtained suspension. An ice bath was employed to control the temperature below 5 °C. An AHM solution was subsequently dropped onto the suspension with an molar ratio of aniline/Mo of 4:1 followed by introducing 1 g of ammonium persulfate (APS) as the initiator. After that, the suspension was left stirring for 24 h and treated with a centrifuge/washing process for 3 times followed by a freeze-drying treatment. The dried precursor was first grounded and transferred to a tube furnace and annealed at 900 °C with a ramping rate of 5 °C min^{-1} in N_2 for 3 h. The Mo−N−C-4-900 was finally obtained by an etching treatment in 2 M NaOH solution at 92 °C for 6 h and 1 M HNO_3 at 50 °C for 1 h followed by a washing and freeze-dry process. Generally, 1 g of Mo−N−C-4-900 can be obtained per batch of synthesis.

Preparations of Mo−N−C-2-900, Mo−N−C-8-900, Mo−N−C-4-800, and Mo−N−C-4-1000. The preparation method is similar to Mo−N−C-4-900 except that, for Mo−N−C-2-900 and Mo−N−C-8-900, the molar ratio of aniline/Mo was changed to 2:1 (Mo−N−C-2-900) and 8:1 (Mo−N−C-8-900). For Mo−N−C-4-800 and Mo−N−C-4-1000, the temperature of the heat treatment was set to 800 (Mo−N−C-4-800) and 1000 °C (Mo−N−C-4-1000).

Preparation of N−C. The preparation method is similar to Mo−N−C-4-900 except that no metal was added. The GO@SiO_2@PANI was directly dried followed by an annealing and etching treatment to afford the N−C.

Preparation of Reduced Graphene Oxide. The rGO was prepared by annealing GO at 400 °C for 2 h under flowing N_2.

Preparation of Co−N−C and Fe−N−C. The preparation of Co−N−C and Fe−N−C samples is similar to that of Mo−N−C with slight modifications. The metal sources used for synthesizing Co−N−C and Fe−N−C are $CoCl_2$ and $FeCl_3$, respectively. In addition, the solutions containing metal, carbon, and nitrogen sources were kept stirring to evaporate the solvent instead of centrifugation and washing processes. The other synthetic process is the same as that of Mo−N−C-4-900.

Preparations of S/Mo−N−C-4-900, S/N−C, and Other Electrodes. The host material (Mo−N−C-4-900, N−C, Mo−N−C-2-900, *etc.*) was mixed with sublimed sulfur with a mass ratio of 1:5 followed by heating in a sealed container at 155 °C under Ar atmosphere for 15 h. After that, the sulfur infused material was further heated in a tube furnace at 200 °C under flowing N_2 for a certain period of time to evaporate excessive sulfur. The preparation method for S/N−C is similar to that of S/Mo−N−C-4-900.

Material Characterizations. The crystal phase of the samples was performed on a XRD diffractometer (PANalytical B.V.) with Cu Kα radiation (λ = 1.5406 Å). The morphology of the samples was observed by scanning electron microscope (Nova NanoSEM 450, 10 kV) equipped with energy-dispersive X-ray (EDX) analyzer and transmission electron microscope (Talos F200X, 200 kV) measurements. The atomic-resolution image of the sample was conducted on aberration-corrected high-angle annular dark-field scanning transmission electron microscope (Titan G2 60-300). The local structure of the samples was determined by the XAS measurement at the beamline 1W2B of the Beijing Synchrotron Radiation Facility (BSRF) of the Institute of High Energy Physics (IHEP) at the Chinese Academy of Sciences (CAS). The S content of the samples was calculated according to the TGA by the TGA8000 analyzer. The surface areas of the samples were calculated by the BET method based on the nitrogen adsorption/desorption isotherms at 77 K with ASAP2000 machine. The element valence state of the samples was obtained by XPS with AXIS-ULTRA DLD-600W analyzer. The LiPS adsorption ability of the samples was evaluated by the UV−vis adsorption test of the solution of 0.01 M Li_2S_4 in DME/DOL (V/V 1:1) which was immersed with the samples and then centrifuged out to form a clear solution.

Electrochemical Measurements. *Preparation of Electrodes for LiPS Redox Conversion and Li_2S Decomposition Tests.* The sample without loading S (*e.g.*, Mo−N−C-4-900) was mixed with sodium alginate in a mass ratio of 4:1 after adding a designed amount of deionized water to form a slurry. The slurry was then casted onto a carbon paper. The active material loaded carbon paper was used as the electrodes for the LiPS transformation test. The asymmetric cell was assembled with the as-prepared electrode as positive electrode, the 0.1 M Li_2S_8-contaning electrolyte as the sulfur source, and the Li foil as the negative electrode.

Preparation of Electrodes for Li−S Battery. The sample was grounded with vapor grown carbon fiber (VGCF), super P, and poly(vinylidene fluoride) (PVDF) with a mass ratio of 80:5:5:10 for 5 min in a mortar. After that, a designed amount of *N*-methyl pyrrolidone (NMP) was added into the mixture to form a uniform slurry. The slurry was further casted onto the surface of carbon-coated aluminum foil followed by drying at 60 °C for 12 h. The S loading of the electrodes was controlled to be *ca.* 2 mg cm^{-2}. The high S loading S/Mo−N−C-4-900 electrode was prepared by mixing S/Mo−N−C-4-900, VGCF, super P, and sodium alginate at a mass ratio of 70:10:10:10 with a designed amount of deionized water and casting the obtained slurry onto nickel foam followed by drying at 60 °C for 12 h. The S loading of the electrodes was controlled to be *ca.* 8 mg cm^{-2}.

The Li−S battery was assembled with the S/host electrode as cathode, lithium foil as anode, and Celgard polypropylene (PP) membrane as the separator. The electrolyte was 1 M LiTFSI dissolved in DME/DOL (v/v 1:1) with 2 wt % $LiNO_3$ as electrolyte. The S/electrolyte ratio is *ca.* 20 for the Li−S battery with a low S loading (2 mg cm^{-2}) and 12 for the one with a high S loading (*ca.* 8 mg cm^{-2}). The voltage range of the cells in the rate performance test was controlled at 1.7−2.8 V for 0.1, 0.2, 0.5, 1 C rates, 1.6−2.8 V for 2, 3, 4 C rates, and 1.5−2.8 V for 5 C rate. As for the long-term cycling performance measurement, the voltage range was controlled to be 1.7−2.8 V. The frequency in the EIS measurement was

https://dx.doi.org/10.1021/acsnano.0c03325
ACS Nano 2020, 14, 10115−10126

controlled in the region of 100,000−0.05 Hz with an AC amplitude of 5 mV.

Calculation Details. The first-principles calculations were performed based on DFT using the projector-augmented wave method as implemented in VASP.[56,57] The exchange and correlation functional was described by generalized gradient approximation with the PBE parametrization.[58−61] Energy cutoffs of 400 and 500 eV for the planewaves were used for the structure optimization and the self-consistent field calculations, respectively. A vacuum region of about 15 Å was used to eliminate interaction of graphene nanoribbon. Brillouin zone is sampled with 3 × 1 × 1 γ-centered k-point mesh. Both lattice constants and atomic positions are optimized with the convergence of energy and force $<10^{-5}$ eV and 0.01 eV/Å, respectively. The adsorption energy was calculated with the equation: $E_{ads} = E(Li_2S_x/substrate) - E(Li_2S_x) - E(substrate)$, with x = 1, 4, 8. The climbing-image nudged elastic band (CI-NEB) method[62] was employed to search the minimum energy paths and locate the transition states during the process of Li_2S decomposition. The convergence force for CI-NEB calculations was set to 0.05 eV/Å.

ASSOCIATED CONTENT

Supporting Information

The Supporting Information is available free of charge at https://pubs.acs.org/doi/10.1021/acsnano.0c03325.

SEM and TEM images of Mo−N−C and N−C; N_2 adsorption/desorption curves and BET surface area and pore size distribution of Mo−N−C, N−C, and rGO; EDS elemental mapping of C, N, O, and Mo for as-prepared Mo−N−C-4-900; TGA curves of S/Mo−N−C and S/N−C; k^3-weighted FT-EXAFS spectrum and corresponding k^3-weighted EXAFS r space fitting curves of Mo−N−C-4-900; SEM images of Mo−N−C-4-900 before and after Li_2S deposition/decomposition; EDS spectra of Mo−N−C-4-900 and N−C electrodes after Li_2S decomposition; discharge/charge profiles and EIS plots of S/N−C, S/Mo−N−C, and S/rGO; SEM images of S/Mo−N−C-4-900 and S/N−C electrodes before and after cycling; cycling performance of S/Mo−N−C-4-900 with high S loading; illustration of the local structure of Mo−N−C-4-900 and N−C; Mo content in Mo−N−C; Mo K-edge EXAFS curve fitting parameters of Mo−N−C-4-900; comparison of the performance of Mo−N−C-4-900; and the results in literatures are provided (PDF)

AUTHOR INFORMATION

Corresponding Author

Qing Li − *State Key Laboratory of Material Processing and Die and Mould Technology, School of Materials Science and Engineering, Huazhong University of Science and Technology, Wuhan, Hubei 430074, China;* orcid.org/0000-0003-4807-030X; Email: qing_li@hust.edu.cn

Authors

Feng Ma − *State Key Laboratory of Material Processing and Die and Mould Technology, School of Materials Science and Engineering, Huazhong University of Science and Technology, Wuhan, Hubei 430074, China;* orcid.org/0000-0002-0856-2783

Yangyang Wan − *Department of Physics and Astronomy, California State University Northridge, Northridge, California 91330, United States*

Xiaoming Wang − *Department of Chemistry and Key Laboratory for Preparation and Application of Ordered Structural Materials of Guangdong Province, Shantou University, Shantou 515063, China*

Xinchao Wang − *Division of Nanomaterials and Chemistry, Hefei National Laboratory for Physical Sciences at the Microscale, CAS Key Laboratory of Materials for Energy Conversion, Department of Materials Science and Engineering, University of Science and Technology of China, Hefei, Anhui 230026, China*

Jiashun Liang − *State Key Laboratory of Material Processing and Die and Mould Technology, School of Materials Science and Engineering, Huazhong University of Science and Technology, Wuhan, Hubei 430074, China*

Zhengpei Miao − *State Key Laboratory of Material Processing and Die and Mould Technology, School of Materials Science and Engineering, Huazhong University of Science and Technology, Wuhan, Hubei 430074, China*

Tanyuan Wang − *State Key Laboratory of Material Processing and Die and Mould Technology, School of Materials Science and Engineering, Huazhong University of Science and Technology, Wuhan, Hubei 430074, China*

Cheng Ma − *Division of Nanomaterials and Chemistry, Hefei National Laboratory for Physical Sciences at the Microscale, CAS Key Laboratory of Materials for Energy Conversion, Department of Materials Science and Engineering, University of Science and Technology of China, Hefei, Anhui 230026, China*

Gang Lu − *Department of Physics and Astronomy, California State University Northridge, Northridge, California 91330, United States*

Jiantao Han − *State Key Laboratory of Material Processing and Die and Mould Technology, School of Materials Science and Engineering, Huazhong University of Science and Technology, Wuhan, Hubei 430074, China*

Yunhui Huang − *State Key Laboratory of Material Processing and Die and Mould Technology, School of Materials Science and Engineering, Huazhong University of Science and Technology, Wuhan, Hubei 430074, China;* orcid.org/0000-0003-1687-1938

Complete contact information is available at: https://pubs.acs.org/10.1021/acsnano.0c03325

Notes

The authors declare no competing financial interest.

ACKNOWLEDGMENTS

This work was financially supported by National Materials Genome Project (2016YFB0700600), National Nature Science Foundation of China (21972051), and the Graduates' Innovation Fund, Huazhong University of Science and Technology (no. 2019ygscxcy031). The work at California State University Northridge was supported by the U.S. National Science Foundation (DMR1828019). The authors thank the Analytical and Testing Center of Huazhong University of Science and Technology (HUST) for carrying out the XPS, SEM, TEM, and TGA measurements.

REFERENCES

(1) Bruce, P. G.; Freunberger, S. A.; Hardwick, L. J.; Tarascon, J.-M. Li−O_2 and Li−S Batteries with High Energy Storage. *Nat. Mater.* **2012**, *11*, 19−29.

(2) Liu, X.; Huang, J. Q.; Zhang, Q.; Mai, L. Q. Nanostructured Metal Oxides and Sulfides for Lithium-Sulfur Batteries. *Adv. Mater.* **2017**, *29*, 1601759.

(3) Mauger, A.; Julien, C. M.; Paolella, A.; Armand, M.; Zaghib, K. A Comprehensive Review of Lithium Salts and Beyond for Rechargeable Batteries: Progress and Perspectives. *Mater. Sci. Eng., R* **2018**, *134*, 1−21.
(4) Zhu, W.; Liu, D.; Paolella, A.; Gagnon, C.; Gariépy, V.; Vijh, A.; Zaghib, K. Application of *Operando* X-Ray Diffraction and Raman Spectroscopies in Elucidating the Behavior of Cathode in Lithium-Ion Batteries. *Front. Energy Res.* **2018**, *6*, 66.
(5) Peng, H. J.; Huang, J. Q.; Cheng, X. B.; Zhang, Q. Review on High-Loading and High-Energy Lithium-Sulfur Batteries. *Adv. Energy Mater.* **2017**, *7*, 1700260.
(6) Li, T.; Bai, X.; Gulzar, U.; Bai, Y. J.; Capiglia, C.; Deng, W.; Zhou, X. F.; Liu, Z. P.; Feng, Z. F.; Zaccaria, R. P. A Comprehensive Understanding of Lithium-Sulfur Battery Technology. *Adv. Funct. Mater.* **2019**, *29*, 1901730.
(7) Chung, S. H.; Chang, C. H.; Manthiram, A. Progress on the Critical Parameters for Lithium-Sulfur Batteries to be Practically Viable. *Adv. Funct. Mater.* **2018**, *28*, 1801188.
(8) Pan, H. L.; Chen, J. Z.; Cao, R. G.; Murugesan, V.; Rajput, N. N.; Han, K. S.; Persson, K.; Estevez, L.; Engelhard, M. H.; Zhang, J. G.; Mueller, K. T.; Cui, Y.; Shao, Y. Y.; Liu, J. Non-Encapsulation Approach for High-Performance Li-S Batteries through Controlled Nucleation and Growth. *Nat. Energy* **2017**, *2*, 813−820.
(9) Hu, Y.; Chen, W.; Lei, T.; Jiao, Y.; Huang, J.; Hu, A.; Gong, C.; Yan, C.; Wang, X.; Xiong, J. Strategies toward High-Loading Lithium−Sulfur Battery. *Adv. Energy Mater.* **2020**, *10*, 2000082.
(10) He, J. R.; Hartmann, G.; Lee, M.; Hwang, G. S.; Chen, Y. F.; Manthiram, A. Freestanding 1T MoS_2/Graphene Heterostructures as a Highly Efficient Electrocatalyst for Lithium Polysulfides in Li-S Batteries. *Energy Environ. Sci.* **2019**, *12*, 344−350.
(11) He, J. R.; Chen, Y. F.; Manthiram, A. Vertical Co_9S_8 Hollow Nanowall Arrays Grown on a Celgard Separator as a Multifunctional Polysulfide Barrier for High-Performance Li-S Batteries. *Energy Environ. Sci.* **2018**, *11*, 2560−2568.
(12) Zhou, G. M.; Sun, J.; Jin, Y.; Chen, W.; Zu, C. X.; Zhang, R. F.; Qiu, Y. C.; Zhao, J.; Zhuo, D.; Liu, Y. Y.; Tao, X. Y.; Liu, W.; Yan, K.; Lee, H. R.; Cui, Y. Sulfiphilic Nickel Phosphosulfide Enabled Li_2S Impregnation in 3D Graphene Cages for Li-S Batteries. *Adv. Mater.* **2017**, *29*, 1603366.
(13) Carbone, L.; Coneglian, T.; Gobet, M.; Munoz, S.; Devany, M.; Greenbaum, S.; Hassoun, J. A Simple Approach for Making a Viable, Safe, and High-Performances Lithium-Sulfur Battery. *J. Power Sources* **2018**, *377*, 26−35.
(14) Marceau, H.; Kim, C.-S.; Paolella, A.; Ladouceur, S.; Lagacé, M.; Chaker, M.; Vijh, A.; Guerfi, A.; Julien, C. M.; Mauger, A.; Armand, M.; Hovington, P.; Zaghib, K. *In Operando* Scanning Electron Microscopy and Ultraviolet−Visible Spectroscopy Studies of Lithium/Sulfur Cells Using All Solid-State Polymer Electrolyte. *J. Power Sources* **2016**, *319*, 247−254.
(15) Paolella, A.; Zhu, W.; Marceau, H.; Kim, C.-s.; Feng, Z.; Liu, D.; Gagnon, C.; Trottier, J.; Abdelbast, G.; Hovington, P.; Vijh, A.; Demopoulos, G. P.; Armand, M.; Zaghib, K. Transient Existence of Crystalline Lithium Disulfide Li_2S_2 in a Lithium-Sulfur battery. *J. Power Sources* **2016**, *325*, 641−645.
(16) Zhu, W.; Paolella, A.; Kim, C. S.; Liu, D.; Feng, Z.; Gagnon, C.; Trottier, J.; Vijh, A.; Guerfi, A.; Mauger, A.; Julien, C. M.; Armand, M.; Zaghib, K. Investigation of the Reaction Mechanism of Lithium Sulfur Batteries in Different Electrolyte Systems by *In Situ* Raman Spectroscopy and *in situ* X-Ray Diffraction. *Sustain. Energy Fuels* **2017**, *1*, 737−747.
(17) Mauger, A.; Julien, C. M.; Paolella, A.; Armand, M.; Zaghib, K. Building Better Batteries in the Solid State: A Review. *Materials* **2019**, *12*, 3892.
(18) Shyamsunder, A.; Beichel, W.; Klose, P.; Pang, Q.; Scherer, H.; Hoffmann, A.; Murphy, G. K.; Krossing, I.; Nazar, L. F. Inhibiting Polysulfide Shuttle in Lithium-Sulfur Batteries through Low-Ion-Pairing Salts and a Triflamide Solvent. *Angew. Chem., Int. Ed.* **2017**, *56*, 6192−6197.
(19) Wang, Y. Z.; Huang, X. X.; Zhang, S. Q.; Hou, Y. L. Sulfur Hosts against the Shuttle Effect. *Small Methods* **2018**, *2*, 1700345.
(20) Ma, F.; Liang, J. S.; Wang, T. Y.; Chen, X.; Fan, Y. N.; Hultman, B.; Xie, H.; Han, J. T.; Wu, G.; Li, Q. Efficient Entrapment and Catalytic Conversion of Lithium Polysulfides on Hollow Metal Oxide Submicro-Spheres as Lithium-Sulfur Battery Cathodes. *Nanoscale* **2018**, *10*, 5634−5641.
(21) Paolella, A.; Demers, H.; Chevallier, P.; Gagnon, C.; Girard, G.; Delaporte, N.; Zhu, W.; Vijh, A.; Guerfi, A.; Zaghib, K. A Platinum Nanolayer on Lithium Metal as an Interfacial Barrier to Shuttle Effect in Li-S Batteries. *J. Power Sources* **2019**, *427*, 201−206.
(22) Tu, S. B.; Zhao, X. X.; Cheng, M. R.; Sun, P. F.; He, Y. W.; Xu, Y. H. Uniform Mesoporous MnO_2 Nanospheres as a Surface Chemical Adsorption and Physical Confinement Polysulfide Mediator for Lithium-Sulfur Batteries. *ACS Appl. Mater. Interfaces* **2019**, *11*, 10624−10630.
(23) Mei, S. L.; Jafta, C. J.; Lauermann, I.; Ran, Q.; Kargell, M.; Ballauff, M.; Lu, Y. Porous Ti_4O_7 Particles with Interconnected-Pore Structure as a High-Efficiency Polysulfide Mediator for Lithium-Sulfur Batteries. *Adv. Funct. Mater.* **2017**, *27*, 1701176.
(24) Liu, J.; Yuan, L.; Yuan, K.; Li, Z.; Hao, Z.; Xiang, J.; Huang, Y. SnO_2 as a High-Efficiency Polysulfide Trap in Lithium−Sulfur Batteries. *Nanoscale* **2016**, *8*, 13638−13645.
(25) Xu, J.; Zhang, W.; Fan, H.; Cheng, F.; Su, D.; Wang, G. Promoting Lithium Polysulfide/Sulfide Redox Kinetics by the Catalyzing of Zinc Sulfide for High Performance Lithium-Sulfur Battery. *Nano Energy* **2018**, *51*, 73−82.
(26) Paolella, A.; Laul, D.; Timoshevskii, V.; Zhu, W.; Marras, S.; Bertoni, G.; Wahba, A. S.; Girard, G.; Gagnon, C.; Rodrigue, L.; Commarieu, B.; Guerfi, A.; Gauvin, R.; Trudeau, M. L.; Vijh, A.; Armand, M.; Zaghib, K. The Role of Metal Disulfide Interlayer in Li−S Batteries. *J. Phys. Chem. C* **2018**, *122*, 1014−1023.
(27) Zhong, Y. R.; Yin, L. C.; He, P.; Liu, W.; Wu, Z. S.; Wang, H. L. Surface Chemistry in Cobalt Phosphide-Stabilized Lithium-Sulfur Batteries. *J. Am. Chem. Soc.* **2018**, *140*, 1455−1459.
(28) Ma, F.; Wang, X.; Wang, J.; Tian, Y.; Liang, J.; Fan, Y.; Wang, L.; Wang, T.; Cao, R.; Jiao, S.; Han, J.; Huang, Y.; Li, Q. Phase-Transformed Mo_4P_3 Nanoparticles as Efficient Catalysts towards Lithium Polysulfide Conversion for Lithium−Sulfur Battery. *Electrochim. Acta* **2020**, *330*, 135310.
(29) Liu, Z. Z.; Zhou, L.; Ge, Q.; Chen, R. J.; Ni, M.; Utetiwabo, W.; Zhang, X. L.; Yang, W. Atomic Iron Catalysis of Polysulfide Conversion in Lithium-Sulfur Batteries. *ACS Appl. Mater. Interfaces* **2018**, *10*, 19311−19317.
(30) Wang, J.; Jia, L.; Zhong, J.; Xiao, Q.; Wang, C.; Zang, K.; Liu, H.; Zheng, H.; Luo, J.; Yang, J.; Fan, H.; Duan, W.; Wu, Y.; Lin, H.; Zhang, Y. Single-Atom Catalyst Boosts Electrochemical Conversion Reactions in Batteries. *Energy Storage Mater.* **2019**, *18*, 246−252.
(31) Lim, W. G.; Mun, Y.; Cho, A.; Jo, C. S.; Lee, S.; Han, J. W.; Lee, J. Synergistic Effect of Molecular-Type Electrocatalysts with Ultrahigh Pore Volume Carbon Microspheres for Lithium-Sulfur Batteries. *ACS Nano* **2018**, *12*, 6013−6022.
(32) Du, Z. Z.; Chen, X. J.; Hu, W.; Chuang, C. H.; Xie, S.; Hu, A. J.; Yan, W. S.; Kong, X. H.; Wu, X. J.; Ji, H. X.; Wan, L. J. Cobalt in Nitrogen-Doped Graphene as Single-Atom Catalyst for High-Sulfur Content Lithium-Sulfur Batteries. *J. Am. Chem. Soc.* **2019**, *141*, 3977−3985.
(33) Li, J.; Chen, C.; Qin, F. R.; Jiang, Y. J.; An, H.; Fang, J.; Zhang, K.; Lai, Y. Q. Mesoporous Co-N-C Composite as a Sulfur Host for High-Capacity and Long-Life Lithium-Sulfur Batteries. *J. Mater. Sci.* **2018**, *53*, 13143−13155.
(34) Zhang, L. L.; Liu, D. B.; Muhammad, Z.; Wan, F.; Xie, W.; Wang, Y. J.; Song, L.; Niu, Z. Q.; Chen, J. Single Nickel Atoms on Nitrogen-Doped Graphene Enabling Enhanced Kinetics of Lithium-Sulfur Batteries. *Adv. Mater.* **2019**, *31*, 1903955.
(35) Hinnemann, B.; Moses, P. G.; Bonde, J.; Jorgensen, K. P.; Nielsen, J. H.; Horch, S.; Chorkendorff, I.; Norskov, J. K. Biornimetic Hydrogen Evolution: MoS_2 Nanoparticles as Catalyst for Hydrogen Evolution. *J. Am. Chem. Soc.* **2005**, *127*, 5308−5309.

https://dx.doi.org/10.1021/acsnano.0c03325
ACS Nano 2020, 14, 10115−10126

(36) Du, Y.; Liu, Z. Y.; Qiao, F. F.; Wang, S. Y.; Chen, K.; Zhang, X. H. Computational Exploration of Reactive Fragment for Mechanism-Based Inhibition of Xanthine Oxidase. *J. Organomet. Chem.* **2018**, *864*, 58−67.
(37) Liu, X. C.; Zhou, S. P.; Liu, M.; Xu, G. L.; Zhou, X. D.; Huang, L.; Sun, S. G.; Amine, K.; Ke, F. S. Utilizing a Metal as a Sulfur Host for High Performance Li-S Batteries. *Nano Energy* **2018**, *50*, 685−690.
(38) Wu, G.; More, K. L.; Johnston, C. M.; Zelenay, P. High-Performance Electrocatalysts for Oxygen Reduction Derived from Polyaniline, Iron, and Cobalt. *Science* **2011**, *332*, 443−447.
(39) Li, Q.; Cao, R.; Cho, J.; Wu, G. Nanocarbon Electrocatalysts for Oxygen Reduction in Alkaline Media for Advanced Energy Conversion and Storage. *Adv. Energy Mater.* **2014**, *4*, 1301415.
(40) Zhang, X. Y.; Yang, Y. Y.; Li, Z. M.; Wang, X. T.; Wang, W. B.; Yi, Z.; Qiang, L. L.; Wang, Q.; Hu, Z. A. Polyaniline-Intercalated Molybdenum Disulfide Composites for Supercapacitors with High Rate Capability. *J. Phys. Chem. Solids* **2019**, *130*, 84−92.
(41) Ren, J. T.; Chen, L.; Weng, C. C.; Yuan, G. G.; Yuan, Z. Y. Well-Defined Mo_2C Nanoparticles Embedded in Porous N-Doped Carbon Matrix for Highly Efficient Electrocatalytic Hydrogen Evolution. *ACS Appl. Mater. Interfaces* **2018**, *10*, 33276−33286.
(42) Gao, Q. S.; Wang, S. N.; Fang, H. C.; Weng, J. W.; Zhang, Y. H.; Mao, J. J.; Tang, Y. One-Dimensional Growth of MoO_x-Based Organic-Inorganic Hybrid Nanowires with Tunable Photochromic Properties. *J. Mater. Chem.* **2012**, *22*, 4709−4715.
(43) Wu, G.; Santandreu, A.; Kellogg, W.; Gupta, S.; Ogoke, O.; Zhang, H. G.; Wang, H. L.; Dai, L. M. Carbon Nanocomposite Catalysts for Oxygen Reduction and Evolution Reactions: From Nitrogen Doping to Transition-Metal Addition. *Nano Energy* **2016**, *29*, 83−110.
(44) Choi, J. M.; Kim, S. H.; Lee, S. J.; Kim, S. S. Effects of Pressure and Temperature in Hydrothermal Preparation of MoS_2 Catalyst for Methanation Reaction. *Catal. Lett.* **2018**, *148*, 1803−1814.
(45) Wu, J. J.; Ma, L. L.; Samanta, A.; Liu, M. J.; Li, B.; Yang, Y. C.; Yuan, J. T.; Zhang, J.; Gong, Y. J.; Lou, J.; Vajtai, R.; Yakobson, B.; Singh, A. K.; Tiwary, C. S.; Ajayan, P. M. Growth of Molybdenum Carbide-Graphene Hybrids from Molybdenum Disulfide Atomic Layer Template. *Adv. Mater. Interfaces* **2017**, *4*, 1600866.
(46) Miao, Z.; Wang, X.; Tsai, M.-C.; Jin, Q.; Liang, J.; Ma, F.; Wang, T.; Zheng, S.; Hwang, B.-J.; Huang, Y.; Guo, S.; Li, Q. Atomically Dispersed Fe-N_x/C Electrocatalyst Boosts Oxygen Catalysis *via* a New Metal-Organic Polymer Supramolecule Strategy. *Adv. Energy Mater.* **2018**, *8*, 1801226.
(47) Chen, W. X.; Pei, J. J.; He, C. T.; Wan, J. W.; Ren, H. L.; Zhu, Y. Q.; Wang, Y.; Dong, J. C.; Tian, S. B.; Cheong, W. C.; Lu, S. Q.; Zheng, L. R.; Zheng, X. S.; Yan, W. S.; Zhuang, Z. B.; Chen, C.; Peng, Q.; Wang, D. S.; Li, Y. D. Rational Design of Single Molybdenum Atoms Anchored on N-Doped Carbon for Effective Hydrogen Evolution Reaction. *Angew. Chem., Int. Ed.* **2017**, *56*, 16086−16090.
(48) Wang, R.; Yang, J. L.; Chen, X.; Zhao, Y.; Zhao, W. G.; Qian, G. Y.; Li, S. N.; Xiao, Y. G.; Chen, H.; Ye, Y. S.; Zhou, G. M.; Pan, F. Highly Dispersed Cobalt Clusters in Nitrogen-Doped Porous Carbon Enable Multiple Effects for High-Performance Li-S Battery. *Adv. Energy Mater.* **2020**, *10*, 1903550.
(49) Han, L.; Liu, X.; Chen, J.; Lin, R.; Liu, H.; Lü, F.; Bak, S.; Liang, Z.; Zhao, S.; Stavitski, E.; Luo, J.; Adzic, R. R.; Xin, H. L. Atomically Dispersed Molybdenum Catalysts for Efficient Ambient Nitrogen Fixation. *Angew. Chem., Int. Ed.* **2019**, *58*, 2321−2325.
(50) Kong, L.; Chen, X.; Li, B. Q.; Peng, H. J.; Huang, J. Q.; Xie, J.; Zhang, Q. A Bifunctional Perovskite Promoter for Polysulfide Regulation toward Stable Lithium-Sulfur Batteries. *Adv. Mater.* **2018**, *30*, 1705219.
(51) Kong, Z.; Li, Y.; Wang, Y.; Zhang, Y.; Shen, K.; Chu, X.; Wang, H.; Wang, J.; Zhan, L. Monodispersed MnO_x-CeO_2 Solid Solution as Superior Electrocatalyst for Li_2S Precipitation and Conversion. *Chem. Eng. J.* **2020**, *392*, 123697.
(52) Zhou, T. H.; Lv, W.; Li, J.; Zhou, G. M.; Zhao, Y.; Fan, S. X.; Liu, B. L.; Li, B. H.; Kang, F. Y.; Yang, Q. H. Twinborn TiO_2-TiN Heterostructures Enabling Smooth Trapping-Diffusion-Conversion of Polysulfides towards Ultralong Life Lithium-Sulfur Batteries. *Energy Environ. Sci.* **2017**, *10*, 1694−1703.
(53) Liu, S. T.; Zhang, C.; Yue, W. B.; Chen, X.; Yang, X. J. Graphene-Based Mesoporous SnO_2 Nanosheets as Multifunctional Hosts for High-Performance Lithium-Sulfur Batteries. *ACS Appl. Energy Mater.* **2019**, *2*, 5009−5018.
(54) Liao, Y. Q.; Xiang, J. W.; Yuan, L. X.; Hao, Z. X.; Gu, J. F.; Chen, X.; Yuan, K.; Kalambate, P. K.; Huang, Y. H. Biomimetic Root-Like TiN/C@S Nanofiber as a Freestanding Cathode with High Sulfur Loading for Lithium-Sulfur Batteries. *ACS Appl. Mater. Interfaces* **2018**, *10*, 37955−37962.
(55) Ma, F.; Zhang, X. Y.; He, P.; Zhang, X. P.; Wang, P.; Zhou, H. S. Synthesis of Hierarchical and Bridging Carbon-Coated $LiMn_{0.9}Fe_{0.1}PO_4$ Nanostructure as Cathode Material with Improved Performance for Lithium Ion Battery. *J. Power Sources* **2017**, *359*, 408−414.
(56) Kresse, G.; Hafner, J. *Ab Initio* Molecular-Dynamics Simulation of the Liquid-Metal-Amorphous-Semiconductor Transition in Germanium. *Phys. Rev. B: Condens. Matter Mater. Phys.* **1994**, *49*, 14251−14269.
(57) Kresse, G.; Furthmüller, J. Efficiency of *Ab Initio* Total Energy Calculations for Metals and Semiconductors Using a Plane-Wave Basis Set. *Comput. Mater. Sci.* **1996**, *6*, 15−50.
(58) Blochl, P. E. Projector Augmented-Wave Method. *Phys. Rev. B: Condens. Matter Mater. Phys.* **1994**, *50*, 17953−17979.
(59) Kresse, G.; Joubert, D. From Ultrasoft Pseudopotentials to the Projector Augmented-Wave Method. *Phys. Rev. B: Condens. Matter Mater. Phys.* **1999**, *59*, 1758.
(60) Perdew, J. P.; Burke, K.; Ernzerhof, M. Generalized Gradient Approximation Made Simple. *Phys. Rev. Lett.* **1996**, *77*, 3865−3868.
(61) Perdew, J. P.; Burke, K.; Ernzerhof, M. Generalized Gradient Approximation Made Simple. *Phys. Rev. Lett.* **1996**, *77*, 3865; *Phys. Rev. Lett.* **1997**, *78*, 1396−1396.
(62) Henkelman, G.; Uberuaga, B. P.; Jónsson, H. A Climbing Image Nudged Elastic Band Method for Finding Saddle Points and Minimum Energy Paths. *J. Chem. Phys.* **2000**, *113*, 9901−9904.

https://dx.doi.org/10.1021/acsnano.0c03325
ACS Nano 2020, 14, 10115−10126